Journal of Power Sources 204 (2012) 249–256

Contents lists available at SciVerse ScienceDirect

Journal of Power Sources

journal homepage: www.elsevier.com/locate/jpowsour

Efficiency improvement and full characterization of dye-sensitized solar cells with MWCNT/anatase Schottky junctions

Simone Quaranta[a], Daniele Gozzi[a], Mario Tucci[b], Laura Lazzarini[c], Alessandro Latini[a,*]

[a] Università di Roma "La Sapienza", Dipartimento di Chimica, Piazzale Aldo Moro 5, 00185 Roma, Italy
[b] Research Center Casaccia, ENEA, Via Anguillarese 301, 00123 Roma, Italy
[c] IMEM-CNR, Parco Area delle Scienze 37/A, Località Fontanini, 43010 Parma, Italy

ARTICLE INFO

Article history:
Received 14 July 2011
Received in revised form 5 December 2011
Accepted 6 December 2011
Available online 14 December 2011

Keywords:
Dye-sensitized solar cells
Schottky junction
Multi-walled carbon nanotubes

ABSTRACT

During the past 20 years, dye-sensitized solar cells (DSSCs) emerged and developed as a promising and low cost alternative to traditional photovoltaics. One of the main obstacles to mass-scale introduction of this technology is represented by their relatively modest conversion efficiency. In this paper, the authors propose and verify the possibility of improving the performance of the devices by taking advantage of the spontaneous formation of Schottky-type rectifying junctions between multi-walled carbon nanotubes and anatase nanoparticles in the preparation of DSSC photoanodes. These junctions improve the charge transport toward the anode with respect to the charge recombination phenomena. A model anatase-graphite Schottky diode was also prepared and characterized in order to verify on macroscopic scale the formation of a Schottky-type junction between the two materials. At 0.1 wt% of MWCNTs a 55% increase of efficiency with respect to DSSCs without MWCNTs has been obtained. The role of the optimum concentration of MWCNTs in the photoanode is discussed on the light of the DSSC electrical parameters taken up from various techniques.

1. Introduction

Exactly 20 years ago, in 1991, *Nature* published a paper [1] entitled "A low-cost, high efficiency solar cell based on dye-sensitized colloidal TiO_2 films" by Brian O'Regan and Michael Grätzel, in which, for the first time, a dye-sensitized solar cell with an efficiency useful for practical purposes (7.1–7.9%) was demonstrated. Before this work, though being already known, dye-sensitized devices were nothing more than lab curiosities. This milestone paper triggered a sort of 'chain-reaction' in the scientific community, with an always-increasing number of research teams involved in DSSC R&D. This is attested by the continuous growth of the scientific paper number concerning DSSCs, which passed from 4 in 1991 to 1037 in 2010 (source: SciFinder Scholar). For his work on DSSCs, Grätzel became one of the most cited chemists, and last year he was awarded of the 2010 Millennium Technology Grand Prize [2]. Unfortunately, the enormous amount of scientific and technological work spent during these 20 years for the improvement of DSSCs was not rewarded by a proportional amount of success. In fact, since 1991 the efficiency of DSSCs has been improved by only about 4% (maximum confirmed efficiency [3]: 11.2%) and this value has been obtained [4] in 2006; since then, no higher-efficiency cells have been confirmed. To make things worse, this efficiency has been obtained with a small area device (0.219 cm^2). Real application-sized sub modules do not reach 10% (maximum confirmed efficiency value [3]: 9.9%). After this brief discussion, in which only the efficiency problem has been considered, it emerges clearly that the improvement of DSSCs is a really difficult task, which requires a multidisciplinary effort. This is due to the structure of a DSSC. In fact, though being apparently a really simple object (toy kits are available to make demonstrative cells), its correct operation requires the concerted optimization of some distinct parts, and this concerted optimization has to be done on the nanoscale. These are:

- the dye;
- the semiconductor;
- the transparent electrodes;
- the cathodic catalyst;
- the electrolyte.

The aim of this work is to understand better the beneficial effect that the addition of a small quantity of MWCNTs to the titania pastes used in the fabrication of photoanodes for DSSCs produces on their overall efficiency. It is also well known that the efficiency maximization depends by several parameters and some of them

* Corresponding author. Tel.: +39 0649913161; fax: +39 0649913161.
E-mail address: alessandro.latini@uniroma1.it (A. Latini).

0378-7753/$ – see front matter © 2011 Elsevier B.V. All rights reserved.
doi:10.1016/j.jpowsour.2011.12.009

appear sometimes to be of empirical nature. For these reasons, the scope of this work does not look for realizing the highest efficiency, which is however our final goal, but to demonstrate and to explain the role of CNTs in improving the efficiency maintaining all other experimental conditions the same. Other researchers [5,6] also tested the effect of CNTs. The explanations proposed of the performance improvements are given simply in terms of easier electron transport through the anode (and so lower chances of recombination phenomena), but these arguments seem susceptible of being improved by taking into account the formation of Schottky junctions. On the other side, the justification of the very limited range of beneficial MWCNT concentration in the photoanode, based on the competition with the dye in the light harvesting process, seems quite satisfactory. To give further strength to the hypothesis presented in this work, the authors realized and fully characterized an anatase-graphite diode (AGD) as a macroscopic-scale model of anatase-MWCNT junctions. On the other hand, no experimental data were found in literature concerning such kind of diode.

2. Experimental

2.1. Materials

High purity sintered graphite rods were purchased from IL CARBONIO, Italy. Nanoparticulate fumed titanium dioxide (Aeroxide VP P90) was kindly given as a free sample by Evonik, Germany. Huntsman (Italy) kindly gave the submicrometric anatase powder for scattering layers. Titanium tetrafluoride, titanium tetrachloride (99.9%), Triton X-100, 3-methoxypropionitrile (MPN) (98%), 4-tert butylpyridine (TBP) (96%), anhydrous lithium iodide (99.99%), iodine (99.999%) and N-719 dye (95%) were purchased from Aldrich. 1,2-dimethyl-3-propylimidazolium iodide (DMPII) (>98%) was purchased from Iolitec (Germany). All the reagents were used as received, with the exception of 3-methoxypropionitrile, which was dried over 0.4 nm molecular sieves, and 4-tert butylpyridine, which was vacuum distilled before use. Glass slides ($50 \times 50 \times 3$ mm, sheet resistance 8 Ω sq.$^{-1}$) with one side fluorine-doped tin oxide (FTO) conductive film were purchased from XOP Fisica (Spain). Nitric acid (65%), hydrochloric acid (37%), absolute ethanol and acetone were purchased from Carlo Erba Reagenti. Counter electrodes were platinized by brushing them with Platisol T paint (Solaronix, Switzerland). Cerasolzer CS186 soldering alloy (MBR ELECTRONICS, Switzerland) was used to solder copper wires to FTO glass. MWCNTs were synthesized and characterized in our laboratory as reported in previous works [7–10].

2.2. Cell assembly

2.2.1. Photoanode

FTO glass slides were ultrasonicated for 15 min in a deionised water/detergent solution, then rinsed with deionised water and ethanol. After this treatment, they were immersed in a 40 mM $TiCl_4$ solution in ultrapure water (resistivity 18 MΩ cm) at 70 °C for 30 min. Then they were rinsed again with deionised water and ethanol. On these treated slides, 1 cm^2 double layer TiO_2 films (transparent + scattering) were deposited by the doctor blade method. For the transparent layer, 120 mg of P90 (pure or mixed with MWCNTs) were dispersed with 1 drop of ultrapure water and 1 drop of 5% HNO_3 in a porcelain mortar and then added of 0.16 ml of ultrapure water, 1 drop of Triton X-100 and mixed until a low viscosity, uniform dispersion is obtained. This first paste is deposited and then the resultant film is dried for 5 min at 125 °C. The scattering layer is then deposited when the slide has cooled down to room temperature. The paste for this layer was prepared by dispersing 50 mg of Huntsman anatase and 5 mg of P90 with 1 drop of ultrapure water and 1 drop of 5% HNO_3 in a porcelain mortar and then added with ultrapure water drop by drop and 1 drop of Triton X-100 under mixing until a paste with a viscosity similar to the previous one. The films were then sintered in air following a sequence of thermal treatments: 325 °C for 5 min, 375 °C for 5 min, 450 °C for 15 min and 500 °C for 15 min. This last treatment was replaced by a 15 min extension of the treatment at 450 °C in the case of MWCNT-containing samples in order to avoid their combustion. After the sintering process, another $TiCl_4$ solution and washing treatment identical to the former was performed, followed by a final thermal treatment at 500 °C (450 °C for MWCNT-containing samples) in air for 30 min. When still relatively hot (70–80 °C), the films were sensitized with the N-719 dye using the fast sensitization procedure developed by Nazeeruddin et al. [11].

2.2.2. Cathode

Two 3 mm holes were drilled into FTO glass slides (for electrolyte filling) and then the slides were washed with deionised water and detergent. Subsequently, they were ultrasonicated for 15 min in a deionised water/detergent solution, then rinsed with deionised water and ethanol, immersed in a 0.1 M HCl solution in ethanol for 5 min, washed with ethanol and finally ultrasonicated in acetone for 10 min. A thermal treatment in air at 400 °C for 15 min followed, in order to remove residual organic contaminants. An area portion of 1 cm^2 of the slide was platinized by brushing it 5 times with Platisol T paint and then heating the slide in air at 400 °C for 15 min.

2.2.3. Cell sealing and electrolyte filling

The DSSC was assembled as a sandwich-type cell and sealed with a 25 μm thick Surlyn hot melt gasket. The space between the cathode and the anode was filled through the holes drilled into the cathode with an electrolyte consisting of a MPN solution 0.1 M LiI, 0.05 M I_2, 0.6 M DMPII and 0.5 M TBP. The holes were then sealed with 60 μm thick Surlyn hot melt gaskets covered by thin glass microscope slides.

2.3. Schottky-type AGD

A 3 mm thick disc was cut from a 30 mm diameter graphite rod, then ultrasonicated with acetone and dried. The disc surface was activated by immersing it for a few minutes in hot 65% HNO_3, then it was washed with deionised water and dried. The anatase coating was obtained as follows. The disc was immersed in a beaker containing a 0.04 M solution of TiF_4 in water, sealed with parafilm, then the beaker was immersed in an ultrasonic bath for 30 min; after it was kept at 60 °C for 20 h, then washed with deionised water and dried in air at 100 °C. This procedure was repeated 2 more times (with the exception of the ultrasonication). Over the anatase coating, a 500 nm thick aluminium layer was deposited by magnetron sputtering, and over the aluminium coating a platinum wire was soldered using a silver loaded conductive paint (RS Components).

2.4. X-ray diffraction

By using a Panalytical X'Pert PRO diffractometer (Cu Kα radiation, $\lambda = 0.154184$ nm) equipped with powder and thin film optics the X-ray diffraction measurements were performed. The detectors of both optics are gas-filled proportional counters. For powder analyses, θ–θ scans were performed, using an incident beam slit of 1° coupled with a 10 mm mask, a collimator of 0.04 rad and a Ni filter for the Kβ component of the Cu radiation. For the diode, a 2θ scan was performed, with a fixed incident beam angle of 1.5°. This type of scan is preferred for thin films in order to suppress the substrate contribution to the diffraction patterns. In this case, an incident

beam slit of 0.03125° coupled with a 10 mm mask and a collimator of 0.04 rad were used. In this case, the Ni filter is not necessary being the thin film optics equipped with a graphite monochromator on the detector arm. The diffraction patterns were collected in the angular range from 20 to 90°. Once collected, the diffractograms of the powders were analyzed using the MAUD Rietveld software package. From the Rietveld analysis, phase composition and refined unit-cell parameters were obtained. The Rietveld refinement is not possible in the case of 2θ-type scans because of the particular type of the diffraction geometry used. In this case, only an estimation of the size of crystallite is given by making use of the Scherrer formula.

2.5. BET specific surface area measurements

BET specific surface area (SSA) of VP P90 was measured by using a Quantachrome Monosorb single point system.

2.6. Scanning electron microscopy

SEM analysis was performed on the diode cross-section with a Zeiss-Leo 1450 VP (resolution 3 nm) in backscattered electrons imaging mode (atomic number contrast) in order to better discriminate the film from the substrate.

2.7. Transmission electron microscopy

Transmission electron micrographs were acquired with a Jeol JEM 2200 FS field emission, energy filtered transmission electron microscope (point resolution: 0.19 nm).

2.8. Solar conversion efficiency measurements

I–V curves under illumination of DSSCs were acquired by using a system composed by a class A solar simulator (Oriel) producing a one sun (1000 W m^{-2}) AM 1.5 G emission, a Keithley 2000 digital multimeter and a data acquisition software written in Visual Basic. Voltage bias is regulated in the range from +850 to −500 mV with steps of 25 mV. Shunt and series resistances were obtained by the slope method near the short circuit and open circuit points, respectively.

2.9. Incident photon to current efficiency (IPCE) measurements

Monochromatic illumination onto the photoanode side of the device for IPCE analysis was performed through the excitation of the cell by a xenon lamp faced to the monochromator. The chopper rotation frequency of the monochromator system was set at 10 Hz. This frequency is different from the frequency used in Si cell and the "resonant condition" due to the capacitive and inductive components typical of DSSCs can be matched. Such arrangement maximizes the signal coming out from the cell. The photocurrents were collected under short circuit conditions in 20 nm increments.

2.10. Electrical characterization

Electrochemical impedance spectroscopy (EIS) was performed with a Solartron 1260A frequency response analyzer. Cells were measured in two-electrode configuration in the dark under a DC forward bias of 300 mV with 10 mV AC perturbation over a frequency range from 10 mHz to 10 kHz. Zview equivalent circuit modelling software was used to fit data by utilizing an equivalent circuit model based on the electrical transmission line theory. The average value of χ^2 was 6×10^{-4}. Some simplifications can be brought to this scheme. The relatively small AC amplitude and DC bias level should ensure a small contribution to the total impedance of the cell due to the mass transport phenomena in the solution

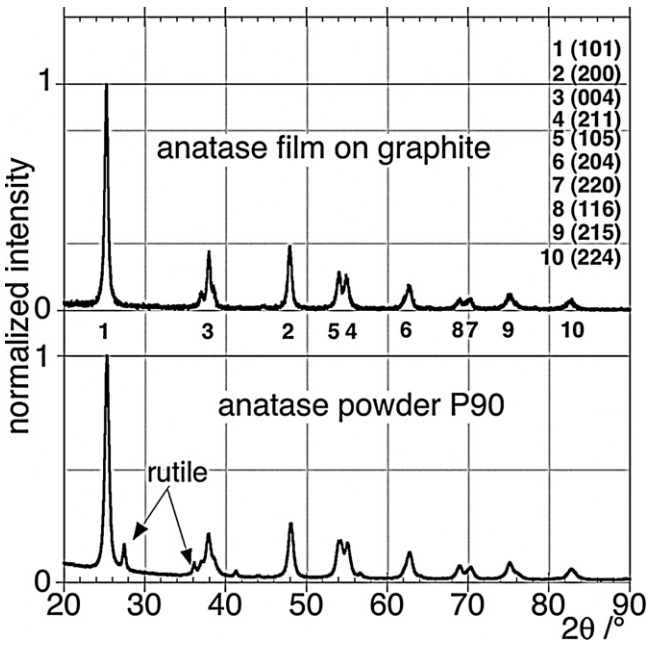

Fig. 1. XRD spectra of nanostructured anatase from different sources for two distinct applications. Top panel: anatase film on graphite obtained by hydrolysis of TiF_4 for realizing the anatase/graphite Schottky diode (AGD). Bottom panel: anatase powder Aeroxide VP 90 by Evonik (Germany) for preparing the transparent film of the DSSC photoanode.

(limited by the anatase nanopores filled with electrolyte). In addition, the formation of a blocking layer on the FTO glass, achieved by the $TiCl_4$ treatment is expected to minimize the charge transfer toward the electrolyte. Photovoltage decays were measured under open circuit voltage conditions with a 530 nm green LED driven by a TTL circuit under the control of a function generator. The cells were brought to a stationary voltage (between 0.4 and 0.6 V) through illumination and then the light excitation is quickly removed while monitoring the decay of the open circuit voltage. Data were acquired on a PC running a program under LabView platform.

3. Results and discussion

The X-ray diffraction patterns reported in Fig. 1 refer, respectively, to Aeroxide VP P90 powder (bottom panel) and film (top panel) deposited on graphite to realize the Schottky diode. The pattern of VP P90 clearly demonstrates that the material is biphasic, containing anatase and rutile whereas the film on graphite is constituted by pure anatase, being the latter prepared TiF_4 hydrolysis as reported before. The Rietveld analysis reveals that the composition is 10.0 ± 0.1 wt% rutile, the remaining being anatase, having the latter an estimated particle size of ∼20 nm. Anatase, which is the phase of interest in the dye-sensitized solar cells, possesses a tetragonal structure (space group *I*41/*amd*, no. 141 [12]). The refined parameters of the anatase unit cell are: a = 0.37854 nm; c = 0.94994 nm both ones in excellent agreement with the reference data. In the case of the film, the estimation of particle size (by the application of the Scherrer equation) gave the same result as above, i.e. ∼20 nm.

The specific surface area of P90 titanium dioxide is quite high if one considers that no internal pores (see TEM images) are present, i.e., 94 ± 2 m^2 g^{-1}. Transmission electron micrographs (Figs. 2 and 3) reveal that P90 TiO_2 is constituted of well-separated, non-porous nanocrystals with dimensions ranging from ∼10 to ∼30 nm, thus confirming the results of the XRD analysis. This particular TiO_2 sample was preferred over the classical 'benchmark' commercial TiO_2, i.e., the Evonik/Degussa P25 since though being

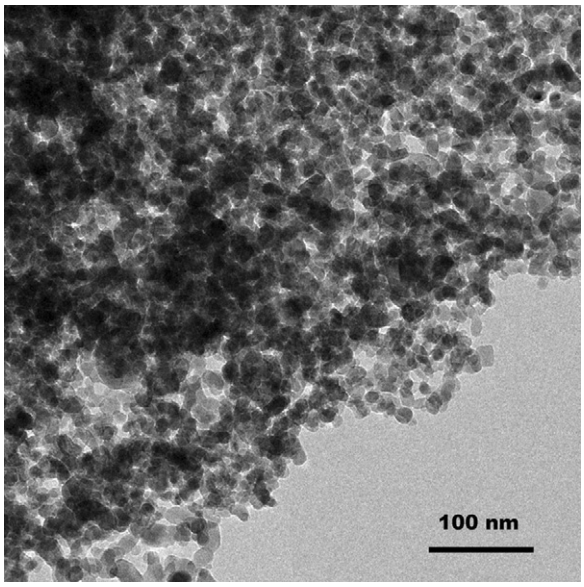

Fig. 2. HR-TEM micrograph of the anatase powder (Aeroxide VP 90 by Evonik, Germany) utilized for preparing the anatase transparent film of the DSSC photoanode.

produced with the same process (the 'Aerosil' process), it possesses a substantially higher SSA (SSA of P25 is $42 \pm 1\ m^2\ g^{-1}$). This property transfers into two big advantages. First one, higher SSA makes P90 more reactive, thus facilitating the sintering of the photoanode and consequently lower temperatures for the thermal treatments can be adopted. This is particularly important for MWCNT-containing photoanodes, to avoid the combustion of MWCNTs. Second one, higher SSA allows for the absorption of larger amounts of dye for device unit area, and so the radiation harvesting improves. This was confirmed, during a preliminary work, in which the amount of N-719 dye absorbed by 1 cm^2-photoanodes made of different TiO_2 samples was measured by ICP spectroscopy: the anode made of P90 absorbed an amount of dye more than double with respect to the anode made of P25 on an electrode surface basis (0.134 ± 0.003 mg vs. 0.066 ± 0.003 mg per 1 cm^2 electrodes).

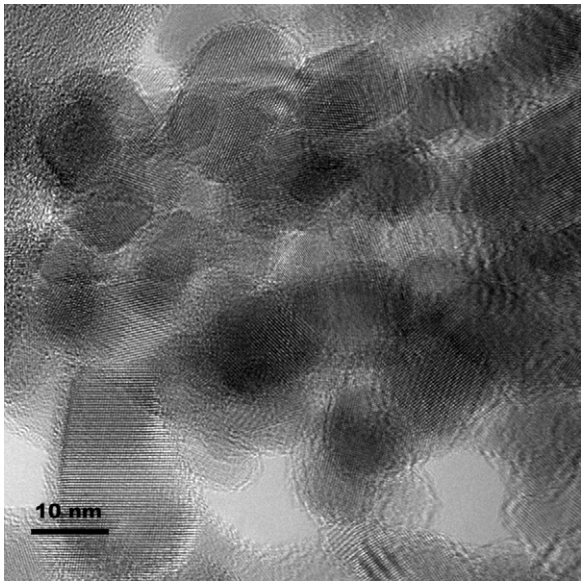

Fig. 3. Magnification of the powder displayed in Fig. 2. The morphology of the anatase nanoparticles is clearly visible and they are well separated and non-porous. The particle size is in the range from ≈10 to 30 nm.

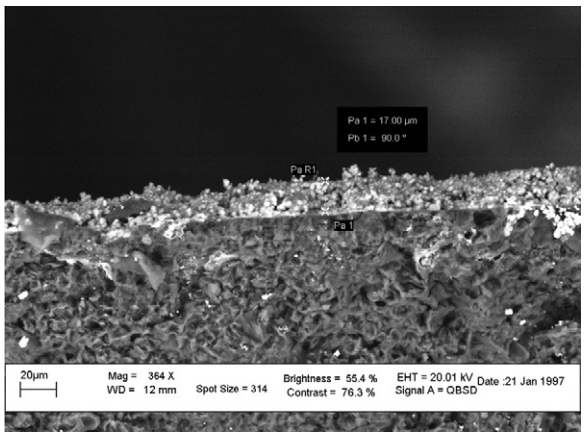

Fig. 4. Cross-section of the junction graphite/anatase of the Schottky diode. Graphite is the bottom grey layer. The thickness of the anatase film is ≈17 µm.

The better performances of P90 with respect to P25 in DSSCs have been already demonstrated in literature [13].

The SEM image of the cross-section of the AGD (Fig. 4) shows an adherent and porous anatase coating with a dense texture with thickness of about 17 µm. The particles that constitute the film are quite monodisperse and well interconnected, having size in the µm-range. This apparent discrepancy with the crystallite dimensions estimated by XRD can be easily explained by considering that these particles are likely polycrystals.

To evaluate the unidirectional conduction produced by the Schottky junction (see scheme in Fig. 5) and barrier height Φ_B in

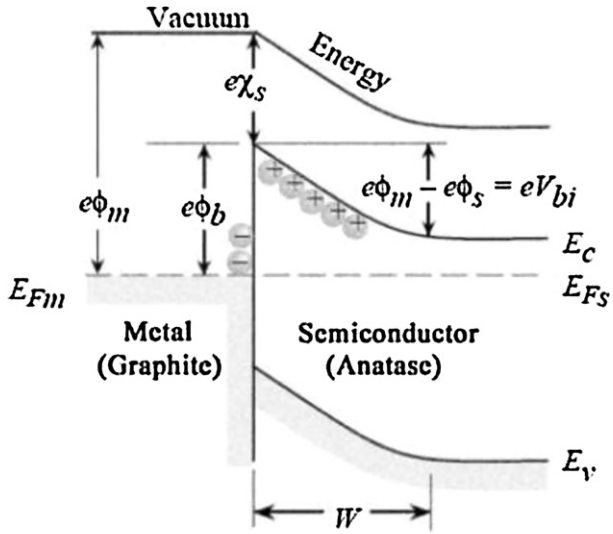

$e\chi_S$=semiconductor electron affinity
$e\phi_m$=metal work function
$e\phi_S$=semiconductor work function
$e\phi_S$=Schottky barrier height
eV_{bi}=contact potential
E_c=conduction band edge energy
E_v=valence band edge energy
E_{Fm}=metal Fermi energy
E_{Fs}=semiconductor Fermi energy
W=depletion layer width

Fig. 5. Schematics of the energy levels for the AGD diode junction structure.

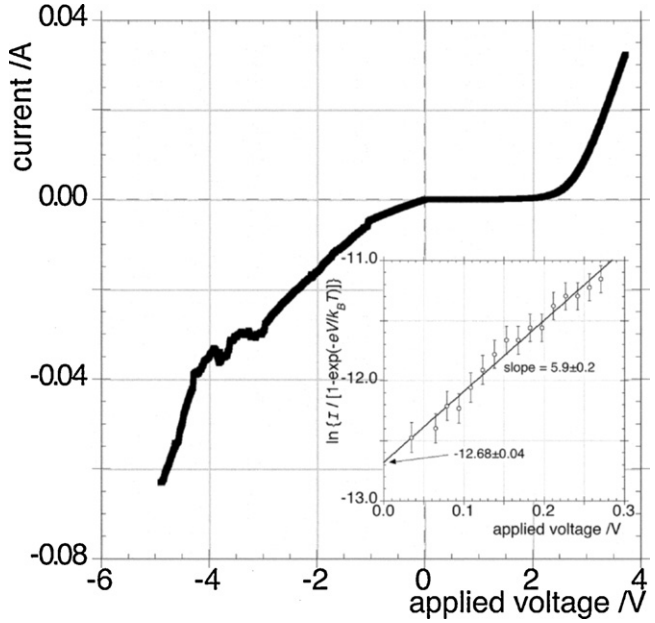

Fig. 6. Polarization curve of the anatase/graphite Schottky diode. The insert shows the low voltage portion of the forward bias plotted as $\ln[I/(1-e^{-eV/nk_BT})]$ vs. V from which the saturation current, I_0, (through the intercept) and ideal factor, n (through the slope) were obtained.

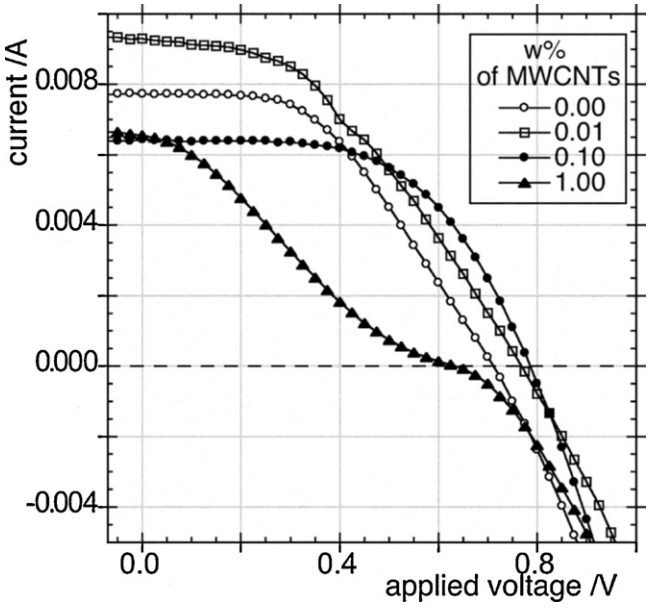

Fig. 7. Polarization curves under *one sun* (AM 1.5 G) illumination of DSSCs having different contents of MWCNTs in the photoanode.

AGD, the polarization curve was recorded and plotted in Fig. 6. The typical rectifying action of a Schottky diode is displayed with ≈2 V voltage offset, V_{offs}. The nanostructured nature of semiconductor and its high band gap could justify this value which is higher than the on the market Si/Au diodes having some hundreds of mV. The polarization curve is represented by equation [14]

$$I = I_0(e^{eV/nk_BT} - 1) \quad (1)$$

where e and k_B are respectively the elementary charge and the Boltzmann constant. n is a factor equal to 1 in the ideal case, which incorporates all those unknown effects that make the device non-ideal. A Schottky diode is unlikely to be uniform over its entire area. Barrier height patchiness leads to $n > 1$ and also explains other effects such as n decreasing with temperature and increasing with reverse bias [15]. The saturation current, I_0, is given by

$$I_0 = aAT^2 e^{-e\Phi_B/k_BT} \quad (2)$$

being a is the junction surface area and A is the Richardson constant. As expected by the basic Schottky theory, that does not consider [16] the Fermi level pinning, diffusive phenomena, electric field drift in the semiconductor depletion layer and doping depending tunnel effects, a leakage current or saturation current should be present in the reverse polarization curve. In the present case, no saturation current was found but a well-defined dependence I vs. V. Such behaviour of the reverse bias can be explained in terms of charge image, which is responsible of the Φ_B decrease through equation

$$\frac{d\Phi_B}{dV} = KN_D\left(\Phi_B - V - \Phi_C - \frac{k_BT}{e}\right) \quad (3)$$

where K, N_D and Φ_C are a constant, the concentration of donor defects and potential difference between the bottom of the conduction band and Fermi level. Though Eq. (3) cannot be calculated because the N_D and Φ_C parameters are unavailable for our nanostructured anatase, the evaluation of Φ_B is feasible. Among the experimental procedures reported in literature [14,17], the extrapolation at $V = 0$ of the forward polarization curve is reliable in the bias range where the voltage drop due to series and shunt resistances can be considered negligible. The plot $\ln[I/(1-e^{-eV/nk_BT})]$ vs. V (see insert in Fig. 6) allows to determine the ideality factor n and I_0 according to Eq. (1) and Φ_B value through equation

$$\Phi_B = \frac{k_BT}{e}\ln\frac{aAT^2}{I_0} \quad (4)$$

as expected by applying Eq. (2). Therefore, being $I_0 = 3.1 \pm 0.1$ μA and by considering $a = 7.068 \times 10^{-4}$ m^2, $T = 291$ K and the Richardson constant [18] $A = 6.71 \times 10^6$ A m^{-2} K^{-2}, $\Phi_B = 0.81$ V. From the slope of linear plot in the insert of Fig. 6, n has been found equal to 6.8. Looking at the SEM picture of Fig. 4, it appears clear that our diode cannot rely on an epitaxial grown junction and thus the n value is consistent with such inhomogeneous graphite-anatase interface. The value of Φ_B is comparable with similar barriers of nanostructured anatase with noble metals such as Au [19], Pt [20], Pd [21] where Φ_B is 0.9, 1.0 and 0.85 eV, respectively. Since the work function of graphite [22] is 5.1 eV, lower than the above metals [23], as first approximation the found Schottky barrier equal to 0.81 eV can be considered in good agreement. The average work function of MWCNTs is reported [22] to be 5.0 eV thus from the point of view of the electronic properties no difference should exist with graphite.

Fig. 7 shows the polarization curves under *one sun* illumination of DSSCs without and with MWCNTs in the photoanode. All the cells were prepared in the same way and with the same materials and they differ only by the MWCNTs concentration in anatase. Looking at Fig. 7 and by Table 1, the considerations below can be drawn:

With exception of the highest MWCNT concentration, the DSSCs containing MWCNTs show higher V_{OC} with respect to the reference cell. In general, a lowering of V_{OC} should be caused by the narrowing of the difference between the Fermi levels of anatase and electrolyte due to the formation of the Schottky barrier between MWCNTs and anatase. The V_{OC} increase can be attributed to the lowering of the dark current caused by MWCNTs according to relationship $V_{OC} = \frac{k_BT}{e}\ln((I_{sc}/I_{dark}) + 1)$ where I_{sc} and I_{dark} are respectively the short circuit and dark current at $V = 0$. While the decrease of I_{dark} and increase of V_{OC} are consistent with faster transport of electrons via MWCNTs in the photoanode, the values found for the highest MWCNT concentration should be explained

Table 1
DSSCs performances as function of MWCNT content in the photoanode.

MWCNT/wt%	V_{OC}/V	I_{sc}/mA	I_{dark}/fA	FF/%	η/%	R_s/Ω	R_{sh}/Ω
0.00	0.737	7.70	1.3	46.32 ± 0.03	2.547 ± 0.007	46	5679
0.01	0.796	9.29	0.15	22.10 ± 0.02	1.010 ± 0.001	30	1981
0.10	0.806	6.41	0.07	56.56 ± 0.05	3.948 ± 0.005	15	4065
1.00	0.711	6.54	3.1	39.88 ± 0.06	3.199 ± 0.004	44	5154

by the catalytic action of the carbon nanostructures on the recombination reaction with the electrolyte.
It is worth noticing that the DSSC at 1 wt% MWCNTs shows a clear rectifying behaviour just crossing the zero current (see Fig. 7). This is a strong support to the formation of a Schottky barrier but at the same time it is proven that an excess of MWCNTs deteriorates the cell performances (fill factor, FF, 22.1%, see Table 1) essentially caused by their competition with dye in absorbing the radiation in addition to the increment of the recombination rate.
Similarly to the Shockley equivalent circuit for a polycrystalline silicon cell in which the fill factor, FF, is defined as

$$FF = FF_0\left(1 - \frac{R_s}{R_{ch}}\right) \quad \text{and} \quad FF = FF_0\left(1 - \frac{R_{ch}}{R_{sh}}\right) \tag{5}$$

where FF_0 is the fill factor of a cell without any parasitic resistance. R_{ch}, R_s and R_{sh} are the characteristic (that is, the reciprocal value of the slope at knee point of the polarization curves of Fig. 7) series and shunt resistances, respectively. The increase of FF requires low R_s and high R_{sh} values. Considering the DSSCs, the former resistance includes the ohmic drops through the electrolyte, photoanode and FTO substrate; the latter represents the overvoltage charge transfer from anatase to electrolyte [24]. The performance differences observed between cells at 0.01 and 0.1 wt% can be justified mainly in terms of shunt and series resistances. The values are $R_s = 30$; $R_{sh} = 1981\ \Omega$ at 0.01 wt% and $R_s = 15$; $R_{sh} = 4065\ \Omega$ at 0.1 wt%. The equation describing the polarization curve, that is,

$$I = I_{sc} - I_0\left[e^{\frac{e(V-IR_s)}{nk_BT}} - 1\right] - \left(\frac{V + IR_s}{R_{sh}}\right) \tag{6}$$

is thus strongly dependent from the parasitic resistances. Supposing the ideal factor n invariant in Eq. (6) and according to the Table 1 resistance values, the expected I_{sc} order should increase going from 0 to 1 wt% MWCNTs. Looking at Fig. 7, such order is not respected since the effect of the light harvesting of MWCNTs is competing with the dye. Furthermore, notwithstanding the absence of MWCNTs in the reference cell, its R_s value is the highest one but, as expected, its I_{sc} is not the lowest one. The R_s value at 1 wt% is affected by a large uncertainty due to the anomalous behaviour close to the open circuit condition. Similarly to I_{dark}, the catalytic effects coming from MWCNTs justify the R_{sh} trend. In fact, faster collection of electrons toward the external circuit favoured by increasing MWCNTs subtracts charges to the recombination reaction. The so high R_{sh} for the reference cell testifies to the absence of the quoted catalytic effect which is compensated by a slower collection efficiency. Therefore, since the MWCNTs act in opposite directions, the cell-optimized performances require a precise MWCNT content in the photoanode. Another factor responsible of lowering the I_{sc} values, which is independent from the MWCNT concentration, is the high extension of the grain boundary surfaces due to the small size of the anatase nanoparticles. On the other hand, it is mandatory to have SSA as high as possible to maximize the amount of dye absorbed.

The dark current polarization curves are shown in Fig. 8 where the rectifying behaviours of the photoanode/electrolyte interface and FTO/anatase junction are recognizable in the intervals 0.35–1 V and −0.20 to 0.25 V, respectively. The existence of the latter barrier

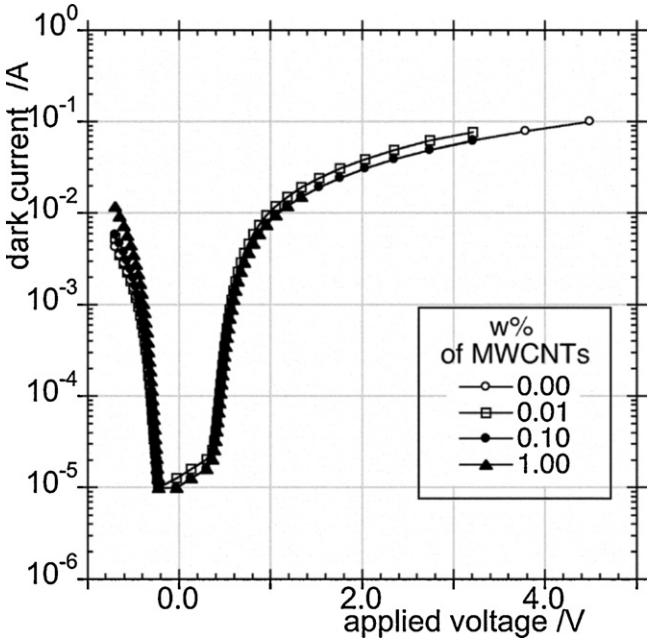

Fig. 8. Polarization curves in the dark of DSSCs having different contents of MWCNTs in the photoanode.

is due to the Fermi level pinning caused by anatase surface defects. It is reported [25] that barriers higher than 0.6 V produce the knee displacement from the ideal position in the polarization curve. Consequently, an efficiency loss occurs. By making use of the recorded data of Fig. 8, the calculated FTO/anatase barrier was found by Eq. (4) equal to 0.73 eV. The corresponding saturation current was equal to 14.0 ± 0.3 μA. The ideality factors extrapolated from the interval 0.4–0.7 V are 1.6 and 2 for the reference cell and for all the MWCNT-containing cells respectively. These values indicate the existence of both diffusion and electron–electrolyte recombination phenomena, but without the predominance of one. A value of 2 for the ideality factor in MWCNT-containing cells can also be indicative of a second-order kinetics for electron–electrolyte recombination.

Fig. 9 displays the IPCE curves as function of MWCNT concentration and the quantum efficiencies at 350 and 530 nm are reported in Table 2. The former wavelength allows evaluate the photoanode radiation harvesting associated to the FTO/anatase interface (see the insert in Fig. 9 where the optical transmission spectra of FTO glass covered by $TiCl_4$ and FTO glass + $TiCl_4$ + anatase P90, see experimental section, are reported) while the latter is particularly significant for the electron transport promoted by the highest dye photogeneration. The beneficial influence of MWCNTs at 350 nm is

Table 2
Incident photon to current efficiency (IPCE) evaluated at 350 nm and 530 nm.

MWCNT/wt%	IPCE (λ = 350 nm)	IPCE (λ = 530 nm)
0.00	0.29	0.45
0.01	0.39	0.57
0.10	0.33	0.42
1.00	0.22	0.31

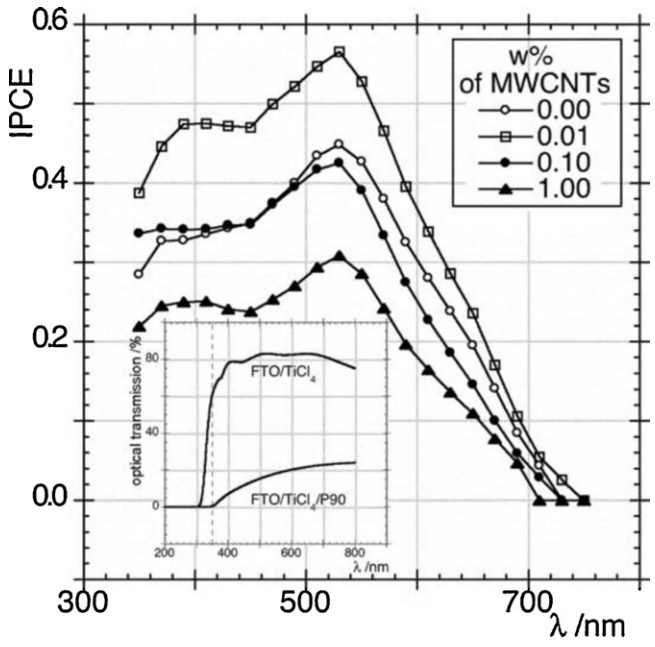

Fig. 9. Incident photon to current efficiency (IPCE) curves of DSSCs having different contents of MWCNTs in the photoanode. The insert shows the optical transmission spectrum of the FTO glass treated with $TiCl_4$ solution and the spectrum of the latter with the anatase layer (as in the photoanode). At 350 nm, the radiation is completely absorbed by the anatase layer. At 530 nm, when the dye is at the absorption maximum, the highest photogeneration occurs.

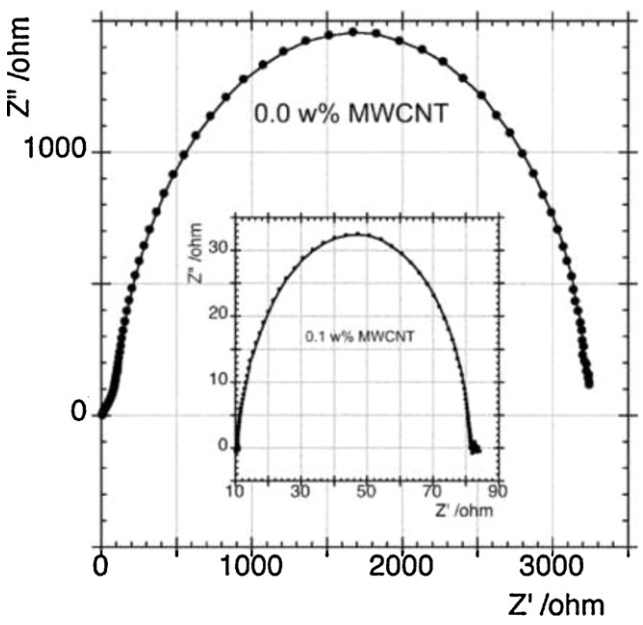

Fig. 10. Nyquist plot of the electrochemical impedance spectrum (EIS) of the DSS reference cell photoanode under 500 mV bias. The insert shows the Nyquist plot of the photoanode containing 0.1 wt% of MWCNTs. The parameters obtained by fitting the EIS spectra are given in Table 3.

probably due to the combined effects of interband excitons generation inside anatase and Schottky barrier, which channels electrons toward MWCNTs. Thus, the recombination hole–electron inside anatase is inhibited. The behaviour at 530 nm can be explained by efficiency terms, η, that contribute to the whole value of IPCE as

$$\mathrm{IPCE} = \eta_{\mathrm{hv}}\eta_{\mathrm{cs}}\eta_{\mathrm{cl}}\eta_{\mathrm{ab}} \quad (7)$$

where the subscripts indicate respectively the radiation harvesting, charge separation, collection and radiation absorption. In DSSCs the harvesting (electron injection from dye to anatase conduction band) is close to unity [26] and the condition of short circuit makes also the charge separation term almost unity [26]. So, as rough approximation, only the last two efficiency terms in Eq. (7) are MWCNT concentration dependent. Looking at Table 2, one figures out that the 0.01 wt% represents a good compromise between the charge transport enhancement (charge extraction time shorter than recombination lifetime [27]) and radiation absorption competition between MWCNTs and dye. On the other hand, the prevailing radiation absorption by MWCNTs at 1 wt% is clearly evident (IPCE value almost halved).

The transport and charge storage parameters of examined DSSCs are reported in Table 3. Typical Nyquist's plots are shown in Fig. 10 for DSSCs without and with MWCNTs (figure and insert, respectively). The impedance plot fits were done according to a simplified transmission model for the DSSC photoanode as proposed in literature [28,29]. The recombination resistance, R_r, which contributes to R_{sh}, is the charge transfer resistance from anatase conduction band to I_3^- in the electrolyte. In fact, its trend is consistent with the values of R_{sh} in Table 1. The marked low values of R_r for cells containing MWCNTs witness the preferential transfer by catalysis of electrons to I_3^-. The effect of metallic component of the carbon nanostructures is clearly evident looking at the electron diffusion resistance, R_d, through the photoanode, if compared with the reference cell. The electron diffusion length, L_n, was calculated according to equation $L_n = L(R_r/R_d)^{1/2}$ in which L is the anatase film thickness assumed 10 μm about for all cells as shown in Fig. 11. The transit time, τ_{tr}, extracted [30] from EIS spectra is the time spent by electrons in crossing the anatase film. Also in this case, it is remarkable the difference between the reference and other cells which is in agreement with higher mobility of electrons in MWCNTs. By the latter parameter, the electron diffusion coefficient, D_n, can be evaluated as $D_n = L^2/\tau_{tr}$. A factor 12 exists in the D_n values between the DSSC, which is the richest in MWCNTs and reference cell. Since the measured diffusion coefficient equal to 1.8×10^{-8} cm^2 s^{-1} of I_3^-, $D_{I_3^-}$, in the photoanode pores filled by electrolyte is lower than D_n, an inductive component appears in the low frequency region of EIS spectra [31,32] (see insert in Fig. 10). This component tends to disappear with the decrease of MWCNT concentration as the difference between D_n and $D_{I_3^-}$ vanishes. The chemical capacitance, C_μ, defined [33] as $C_\mu = e^2(\partial n_i/\partial \mu_i)$, where n_i is the charge carrier density in the anatase and μ_i the chemical potential of electrons, shows the expected decreasing trend of the storage capacity of the

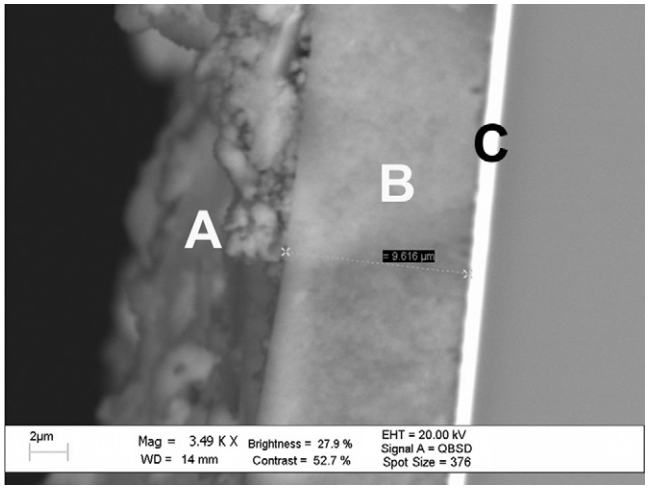

Fig. 11. Cross-section of a DSSC photoanode. Anatase scattering layer made of Huntsman (Italy) anatase powder Anatase transparent layer ≈10 μm thick made of anatase powder Aeroxide VP 90 by Evonik (Germany) FTO glass.

Table 3
Transport and charge storage parameters of DSSCs at different MWCNT concentration obtained by EIS. R_r, R_d, τ_{tr}, D_n, L_n and C_μ are the recombination resistance, diffusion resistance, transit time, electron diffusion coefficient, electron diffusion length and chemical capacitance. The electron lifetime, τ_n, was measured by the OCVD technique.

MWCNT/wt%	R_r/Ω	R_d/Ω	τ_{tr}/ms	$D_n/cm^2\ s^{-1}$	$L_n/\mu m$	C_μ/mF	τ_n/ms
0.00	2848	1020	112	8.85×10^{-8}	16	11	63 ± 16
0.01	57	27	14	7.27×10^{-7}	21	0.22	46 ± 5
0.10	71	16	14	7.28×10^{-7}	15	0.35	35 ± 4
1.00	457	80	7	1.10×10^{-6}	23	2.4	49 ± 7

photoanode when the metallic component increases. The anomalous value at 1.0 wt% could be justified by some superimposition of C_μ with the Helmholtz double layer capacitance localized within the anatase pores.

To evaluate the lifetime of electrons, τ_n, in the photoanode the OCVD technique has been used. In the photovoltage region explored (0.4–0.6 V), this procedure allows to determine the direct recombination (without trapping) between I_3^- and electrons [34]. Data reported in the last column of Table 3 shows that no particular difference exists between reference cell and cells with MWCNTs. These results are reasonable considering the opposite effects acting on the electron lifetime: it grows because of the Schottky barrier and it contracts due to the aided catalytic charge transfer.

4. Conclusions

The results presented in this work state that:

- The macroscopic junction anatase/graphite is a true rectifying junction behaving as Schottky diode. This result has been transferred to the nanostructured junction anatase/MWCNT being the carbon nanostructure graphite like.
- DSSCs realized strictly with the same procedure and materials show electrical and photovoltaic properties changing with the content of MWCNTs in their photoanode.
- The concentration of MWCNTs in the photoanode anatase layer is a critical parameter for obtaining the highest efficiency: low concentrations do not produce appreciable improvements while high concentrations subtract radiation to the photovoltaic conversion because of the black body nature of MWCNTs. Though further work is required to look for the "rightest concentration" of MWCNTs as well as the optimization of other parameters, we obtained at 0.1 wt% of MWCNTs a 55% increase of efficiency with respect to DSSCs without MWCNTs.

Acknowledgments

The authors wish to thank Evonik-Degussa, its italian distributor, Eigenmann and Veronelli, and particularly Dr. Giuseppe Carminati for kindly supplying a free sample of Aeroxide VP P90 titanium dioxide.

References

[1] B. O'Regan, M. Grätzel, Nature 353 (1991) 737–740.
[2] G.J. Meyer, ACS Nano 4 (2010) 4337–4343.
[3] M.A. Green, K. Emery, Y. Hishikawa, W. Warta, Prog. Photovolt: Res. Appl. 19 (2011) 84–92.
[4] Y. Chiba, A. Islam, Y. Watanabe, R. Komiya, N. Koide, L. Han, Jpn. J. Appl. Phys. 45 (2006) L638–L640.
[5] S. Muduli, W. Lee, V. Dhas, S. Mujawar, M. Dubey, K. Vijayamohanan, S.-H. Han, S. Ogale, ACS Appl. Mater. Int. 1 (2009) 2030–2035.
[6] T. Sawatsuk, A. Chindaduang, C. Sae-Kung, S. Pratontemp, G. Tumcharern, Diamond Relat. Mater. 18 (2009) 524–527.
[7] M. Tomellini, D. Gozzi, A. Latini, J. Phys. Chem. C 111 (2007) 3266–3274.
[8] D. Gozzi, M. Iervolino, A. Latini, J. Am. Chem. Soc. 129 (2007) 10269–10275.
[9] D. Gozzi, A. Latini, M. Tomellini, J. Phys. Chem. C 113 (2009) 45–53.
[10] D. Gozzi, A. Latini, L. Lazzarini, Chem. Mater. 20 (2008) 4126–4134.
[11] Md.K. Nazeeruddin, R. Splivallo, P. Liska, P. Comte, M. Grätzel, Chem. Commun. 145 (2003) 6–1457.
[12] JCPDS – International Centre for Diffraction Data, Card 78-2486, 2001.
[13] L. Grinis, S. Dor, A. Ofir, A. Zaban, J. Photochem. Photobiol. A 198 (2008) 52–59.
[14] D.K. Schroder, Semiconductor Material and Device Characterization, 3rd ed., IEEE Press, John Wiley & Sons Inc., 2006.
[15] R.T. Tung, Appl. Phys. Lett. 58 (1991) 2821–2823.
[16] J. Bardeen, Phys. Rev. 71 (1947) 717–727.
[17] T. Dittrich, V. Zinchuk, V. Skryshevskyy, I. Urban, O. Hilt, J. Appl. Phys. 98 (2005), 104501/1–6.
[18] M.C.K. Sellers, E.G. Seebauer, Thin Solid Films 519 (2011) 2103–2110.
[19] E.W. McFarland, J. Tang, Nature 421 (2003) 616–618.
[20] X.Z. Ji, G.A. Somorjai, J. Phys. Chem. B 109 (2005) 22530–22535.
[21] J.Y. Park, J. Renzas, B.B. Hsu, G.A. Somorjai, J. Phys. Chem. C 111 (2007) 15331–15336.
[22] H. Ago, T. Kugler, F. Cacialli, W.R. Salaneck, M.S.P. Shaffer, A.H. Windle, R.H. Friend, J. Phys. Chem. B 103 (1999) 8116–8121.
[23] H.L. Skriver, N.M. Rosengaard, Phys. Rev. B 46 (1992) 7157–7168.
[24] S. Rani, P. Suri, R.M. Mehra, Prog. Photovolt: Res. Appl. 19 (2011) 180–186.
[25] M. Ni, M.H.K. Leung, D.Y.C. Leung, K. Sumathy, Sol. Energy Mater. Sol. Cells 90 (2006) 2000–2009.
[26] A.B.F. Martinson, M.S. Goes, F. Fabregat-Santiago, J. Bisquert, M.J. Pellin, J.T. Hupp, J. Phys. Chem. A 113 (2009) 4015–4021.
[27] M. Grätzel, Inorg. Chem. 44 (2005) 6841–6851.
[28] F. Fabregat-Santiago, G. Garcia-Belmonte, J. Bisquert, A. Zaban, P. Salvador, J. Phys. Chem. B 106 (2002) 334–339.
[29] J. Wu, G. Chen, C. Lu, W. Wu, J.S. Chen, Nanotechnology 19 (2008) 105702.
[30] M. Adachi, M. Sakamoto, J. Jiu, Y. Ogata, S. Isoda, J. Phys. Chem. B 110 (2006) 13872–13880.
[31] I. Mora-Serò, J. Bisquert, F. Fabregat-Santiago, G. Garcia-Belmonte, Nano Lett. 6 (2006) 640–650.
[32] G. Kron, T. Egerter, G. Nelles, A. Yasuda, J.H. Werner, U. Rau, Thin Solid Films 403–404 (2002) 242–246.
[33] J. Bisquert, V.S. Vikhrenko, S. Vyacheslav, J. Phys. Chem. B 108 (2004) 2313–2322.
[34] D. Zhao, T. Peng, L. Lu, P. Cai, P. Jiang, Z. Bian, J. Phys. Chem. C 112 (2008) 8486–8494.